Design, Fabrication and Experimental Validation of a Steerable, Laser-Driven Microrobot in Dry Environments

Zhong Yang, Andriy Sherehiy, Sri Sukanta Chowdhury, Danming Wei, Ruoshi Zhang, Dan O. Popa¹

Abstract— In this paper, we discuss the design and validation methodology of SerpenBot, a laser-driven microrobot that operates in dry environments and can be steered. The microrobot includes a novel resonant leg mechanism that couples with a Nd:YAG pulsing laser beam at tunable frequencies, thus producing differential driving forces that can be selectively used for both driving and turning of the microrobot. Specifically, the SerpenBot includes two micromachined silicon thermal actuators with serpentine design and a motion amplification flexure, that are stimulated using different modulated laser pulse frequencies. We present analysis, simulation, and experimental results demonstrating the successful maneuverability of the SerpenBot on a dry Silicon substrate.

I. INTRODUCTION

Microrobotics has experienced a lot of scientific progress in the last decade and shows promising practical bio and nano applications such as drug delivery, cell manipulation, micro/nano part transport, and assembly. Microrobot fabrication is based on Integrated Circuit (IC) and Micro Electromechanical System (MEMS) technology, where researchers exploit a variety of micro-actuator technologies, such as those based on piezoelectric, electrostatic, or thermal effects. Furthermore, the energy supplied to microrobots can also take different forms, such as vibration, magnetic field, electric field, laser, chemical, and others.

In general, microrobots can be classified as Type-R (Remote-powered) and Type-E (Energy-harvesting) microrobots. A Type-E microrobot can harvest and store energy from the environment, then expend that energy to power actuators and also on-board sensors and controller units. On the other hand, Type-R microrobots can also harvest energy from the environment but they have neither energy storage nor control unit on-board.

Work in [1-4] exploit magnetic fields for moving and operating microrobots as Type-R units. Work in [5] proposes using an electromagnetic field to levitate the microrobot, while actuate the microgripper with laser beam, and this microrobot can be classified as a Type-R microrobot. Researchers at Harvard [6] designed a Type-E microrobot based on piezoelectric actuator, for which the actuation energy is from a carried battery. In [7] the Type-E microrobot also powered by a battery, and actuated by an electrothermal actuator. Furthermore, Robo-Fly from University of Washington [8] was designed by harvesting laser energy for actuating piezoelectric actuators as a classic Type-E microrobot.

In past work, we introduced a novel Type-R microrobot, the ChevBot (Figure 1) [9,10]. ChevBot is a laser-driven

¹Authors are with the Next Generation Systems Group (NGS), Department of Electrical and Computer Engineering, University of Louisville, Kentucky, USA, email: zhong.yang@louisville.edu.

locomotor which is able to navigate through an operating surface following desired trajectories. Our paper [9] saw the first introduction of the concept of modulated laser pulse frequency to control the behavior of the microrobot, and this behavior was predicted using simulations. In [10] the ChevBot was designed using a Chevron Thermal Actuator (CTA), and was fabricated by standard MEMS cleanroom process on the Silicon On Insulator (SOI) wafers. A 532nm Nd:YAG laser beam was used for both driving and controlling the ChevBot's velocity. When the laser spot focuses on the CTA, the thermal expansion is generated, while kinematic constraints of the actuator convert the thermal expansion to displacement of a shuttle containing a microassembled dimple. This microassembled dimple generates a stick and slip motion on a dry, Silicon substrate. Although the ChevBot can locomote on a dry substrate, it is not able to steer and follow trajectories in 3 degrees of freedom (DOF). Because it had only one actuator, the motion of the ChevBot was typically uni-directional, and the robot was turning unpredictably depending on substrate surface conditions.

In this paper, we present a new laser-driven microrobot, the SerpenBot, with serpentine-like actuators and leg designs that allow controllable turning motions in addition to forward and backward velocities. We discuss the novelties of the microrobot design, present simulation and analysis of its predicted behavior, and experimental validation demonstrating steerable trajectories on a Silicon substrate. Experimental results reported here show that SerpenBot is capable of velocities up to 68 microns/s, and angular velocities of 3.8 degrees/s while turning left and right.

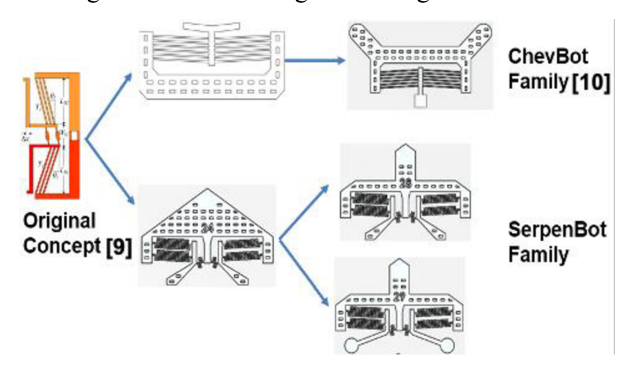


Figure 1. Families of Laser-Driven Microrobot.

II. SERPENBOT DESIGN AND MODELING

Our previous studies have revealed that motion of the laser-driven microrobots strongly depends on the geometry of its body [9,10]. Therefore, design and relative location of the microrobot's components need to be considered to enable locomotion and steering on a flat surface in a controlled way.

Based on the findings from the experiments with the older generation of the laser-driven robots (ChevBots) [9,10,16], we introduced and updated a new laser-driven robot based on both static and dynamic behavior considerations and a design shown in Figure 2. The new driving structure called Elbow Thermal Actuator (ETA) is the modification of Vertical Thermal Actuators (VTA) used in thin-film MEMS actuator designs [11]. Upon heating, the ETA's serpentine structure experiences thermal expansion, thus causing the actuator to supply the motion to the leg mechanism, and as a result, move the body of the microrobot. The actuators of the microrobot are working under a dynamic Opto-Thermo-Mechanical energy conversion process, therefore a multi-physics dynamic analysis of serpentine structure was conducted in order to select appropriate leg designs.

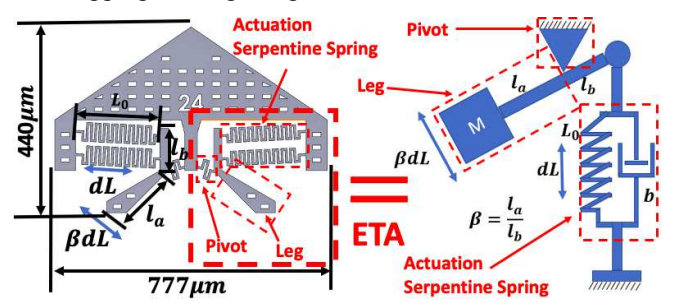


Figure 2. SerpenBot design, based on serpentine actuator and the Elbow Thermal Actuator (ETA).

A. Thermal Expansion and Displacement

The optothermal effect is an increase in temperature of the material upon laser irradiation, which leads to thermal expansion. This effect was utilized in the case of the VTA beam structure [16] and by analogy, it can be applied for the new ETA serpentine geometry. Exposing ETA to the laser energy induces thermal expansion of the structure's components (e.g. the serpentine spring) resulting in the motion of the robot's leg (Figure 2). We can simulate the behavior of the ETA structure and approximate thermal expansion of the serpentine spring with a lumped model. The change in the length of the serpentine spring due to thermal expansion ΔL can be expressed in following way:

$$dL = \alpha L_0 dT, \tag{1}$$

where the α is the thermal expansion coefficient, dT is the temperature change of the ETA structure, and L_0 is the equivalent original length of actuator serpentine spring. The transfer of motion from the serpentine spring to the leg (Figure 2) is enhanced with the help of lever component in ETA design. The enhancement rate is given by:

$$\beta = \frac{l_a}{l_b},\tag{2}$$

where β is the ratio of mechanical leverage, and l_a and l_b is the length of different parts of the lever. Therefore, the displacement of the microrobot's leg dL_L is described by:

$$dL_L = \beta dL = \beta \alpha L_0 dT. \tag{3}$$

B. Actuator Stiffness

In the last section we have modeled the thermal behavior and motion mechanism of the ETA. In this section we determine the spring constant of the ETA based on its geometry. The serpentine geometry greatly influencesthe dynamic behavior of the actuator, because the serpentine shape has less stiffness compared to a beam design with comparable dimensions. Furthermore, the ETAspring constant determines the resonant frequency of the structure. The spring constant of the serpentine spring is a 6 by 6 tensor. However, considering our geometry in which spring thickness is much larger than width and length, we can approximate the dominant x and y directions (Figure 3) of the tensor. Thus, the spring constant of the serpentine spring in x and y direction are given by [12, 13]:

$$k_{x} = \left[\frac{(N+1)l_{o}^{3}}{6EI_{zo}} + \frac{(N+1)l_{o}^{2}l_{p}}{2EI_{zp}} \right]^{-1}, \tag{4}$$

$$k_y = \left[\frac{\left(2(N+2)l_p\right)^3}{3EI_{zp}} + \frac{(8N^3 + 36N^2 + 55N + 27)l_p^2l_o}{3EI_{zo}} \right]^{-1}, (5)$$

where N is the number of times the structure pattern repeats, l_o is vertical beam length, l_p is horizontal beam length, I_{zo} is z-axis moment of inertia of l_o , and I_{zp} is z-axis moment of inertia of l_p , as shown in Figure 3. Through equations (4) and (5), we can design different geometry constants l_o , l_p , and change N to significantly change the spring constant of the actuator. We can use these two formulas to estimate the spring constants of actuators and, later on, induce differential resonance in each leg.

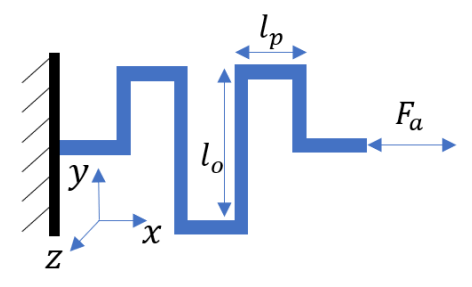


Figure 3. Serpentine spring of the Elbow Thermal Actuator (ETA).

C. Actuator Dynamics

In order to describe the behavior of the actuator in a dynamic situation, we can combine a lumped spring-massdamper system equation with the lever enhancement model. The second order differential equation for ETA can be written

$$M\beta \ddot{L} = F_a - k(L_0 - L) - b\dot{L},\tag{6}$$

 $M\beta \ddot{L} = F_a - k(L_0 - L) - b\dot{L}, \tag{6}$ where *M* is the mass of the leg, F_a is the thermal stress, *k* is the spring constant, L_0 is the equivalent original length of actuator serpentine spring, L is the actuator's length after thermal expansion, \dot{L} and \ddot{L} are the speed and acceleration of the actuator length change, and b is the damping ratio. In this linear second order differential equation, and F_a is generated stress due to the thermal expansion [16]. Therefore, our system is a linear third order system. After applying the Laplace transformation to the differential equation (6), we have determined that the system has three poles on the Laplace domain. One real pole from the thermal behavior, and two poles from the mechanical vibration (Figure 4). This observation can provide us with good guidance for the design of an actuator with given range of frequency.

To actuate and steer the microrobot we use pulsed laser frequency from a single, large laser spot illuminating the SerpenBot. By tuning the pulsed frequency, we can selectively actuate only one of the actuators, left or right, in order to turn the microrobot left or right respectively. Furthermore, both actuators can be activated simultaneously in order to drive the robot along a straight trajectory. Selective activation can be done by tuning modulation frequency of the laser to resonant frequency of each actuator. Therefore, in our proposed design, each SerpenBot has two ETAs with different leg geometries, therefore two resonant frequencies of each leg given by:

$$f = \frac{1}{2\pi} \sqrt{\frac{N_s k}{m}}. (7)$$

Given constraints on the microrobot size and the number of serpentine springs of N_s , we can lower the resonant frequency by increasing the mass of the serpentine structure or decreasing the value of the spring constant. This can be expressed by the pole shift on the complex plane depicted in Figure 4. From the plot (Figure 4) it can be seen that increase of the beam length of the serpentine spring, will shift the two imaginary poles closer to the y axis. On the other hand, the decrease of the robot's body area will decrease its thermal capacity, resulting in increase of the speed of the heating-cooling cycle (shift of real pole - red points in Figure 4).

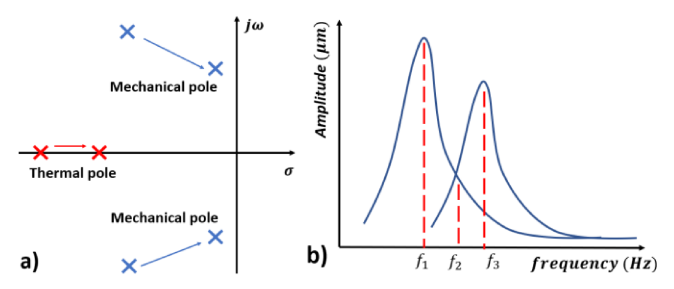


Figure 4. The system transfer function poles motion when increasing the size of the beams of the ETA.

Using the geometry design parameters listed in Table I, we can estimate that the resonant frequencies of the microrobot legs will be separated apart by approximately 1kHz, as shown in Table II.

TABLE I. ANALYTICAL & SIMULATION PRAMETERS

$ ho_{Si}$	Density of Silicon	2328 $(kg \cdot m^{-3})$	
E_{Si}	Si Young's modulus	165 (GPa)	
l_{o-left}	Left vertical beam length	40 μm	
l_{p-left}	Left horizontal beam length	15 μm	
$l_{o-right}$	Right vertical beam length	30 μm	
$l_{p-right}$	Right horizontal beam length	15 μm	
t_b	Beam thickness	5 μm	
h	Device lay thickness	20 μm	
m_{left}	Left actuator mass	0.00069442 μg	
m_{right}	Right actuator mass	0.00077669 μg	
N	Spring number of the structure repeat times	8	
N _s	Actuator serpentine spring number	2	

TABLE II. LEG RESONANT FREQUENCY ESTIMATION

Left	f_{ky}	Left actuator resonant frequency in	86.5 kHz
actuator		y direction	
Right	f_{kv}	Right actuator resonant frequency	87.7 <i>kHz</i>
actuator	,	in y direction	

III. SERPENBOT FEA SIMULATIONS

To better understand the mechanic behavior and to optimize the actuator design, we conducted Finite Element Analysis (FEA) with ANSYS®. In this study, we focus on mechanical structural simulations, while an Opto-Thermo modelinvestigated using FEA is detailed in our past work [16].

A. FEA Static Analysis

The static FEA simulation assume that the SerpenBot is heating to temperatures of 500°C and that the body frame is stationary. The thermal expansion on the serpentine spring determine the resulting motion on the leg. The simulation result shown in Figure 5 demonstrates the static deformation of the ETA and the leg under constant thermal loading, which gives us numerical values of the structure's motion. We have tabulated the resulting average displacement of the structure in Table III.

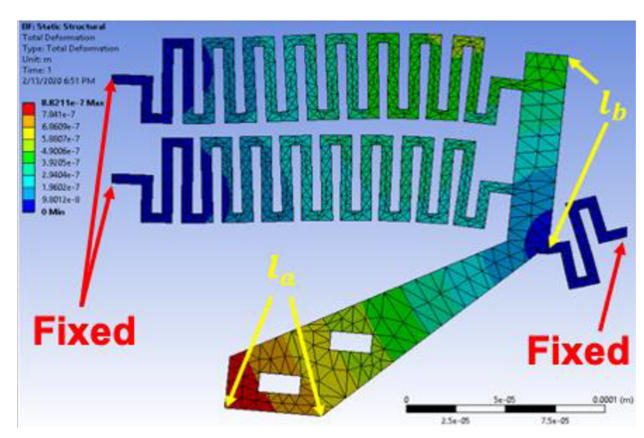


Figure 5. Simulation results indicating deformation of the actuator and the leg, where the end of the serpentine spring and pivot spring is fixed. The arrows indicate the reference points to calculate the average motion.

TABLE III. MOTION OF THE SERPENBOT LEG

	l_a motion (d L) (μm)	l_b motion ($oldsymbol{eta}$ d L) ($oldsymbol{\mu} m$)	β
Left Actuator	0.8318	0.5854	1.4211
Right Actuator	0.8239	0.6125	1.3451

B. FEA Dynamic Analysis

In order to verify the analytic resonance differentiation between the microrobot legs and further optimize the serpentine actuator design, we employ the Modal and Harmonic Response tools in ANSYS® for vibration analysis. When untethered on the substrate, the SerpenBot's frame and legs are free to move and the contact between the legs and substrate's surface can be considered as a hinged joint. But for FEA modeling, this will bring significant complexity to the simulation. To simplify the boundary conditions, we fixed the frame of the microrobot, then apply driving force in order to analyze the vibrational modes of the actuator. The simulation results shown in Figure 6 are based on geometric parameters shown in Table I.

Our simulation-based findings reveal that due to geometry difference, ETAs have multiple different resonant frequencies (Figure 6c). In consequence, because of the different resonant frequencies, specific driving force inputs can activated selectively on only one actuator and leg. Considering realistic experimental conditions due to the hinged joints, we expect the experimental resonant frequency to be lower than the simulation result (Figure 6, Table 1). In this scenario the pulsed laser with respective modulation frequency is similar to the driving force F_a from the simulation model in equation (6). Therefore, when the whole robot is exposed to the laser spot, only one actuator is activated due to matching of the resonant frequency of the ETA and the laser pulse frequency.

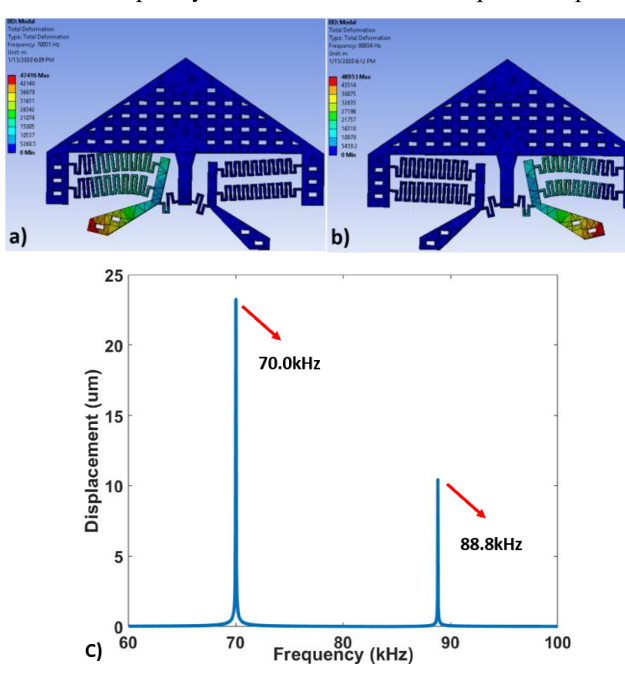


Figure 6. Resonant frequency peaks of the left and right leg of the microrobot.

Furthermore, the analysis only includes information about the actuator and legs of the microrobots, but does not consider the necessary force output to move the frame. In the design shown in Figure 6a, the frame mass is about 11.8 times larger than the legs. As a result, we noted that it may also be necessary to modify the weight distribution of the microrobot to initiate the stick-and-slip motion. Furthermore, the resonance frequencies of the ETAs were estimated using the mass of the leg and actuator while the frame is fixed. Thus, resonant frequency values will undoubtedly be lower once the frame is free to move.

IV. FABRICATION & EXPERIMENTAL SETUP

This section introduces the fabrication steps of the SerpenBot, and the locomotion experiment setup with laser delivery and power regulation system.

A. Cleanroom Fabrication

The SerpenBot is a microrobot based on MEMS technology, and fabricated in cleanroom. The wafer we used to fabricate the SerpenBot is Silicon on Insulator (SOI), with the thickness of the device layer and the buried oxide layer of 20µm and 2µm, respectively. Since we do not pass current

through the silicon nor wet etch, crystal orientation and resistivity of the wafer are not important. The substrate was first cleaned by the RCA process to remove any contamination. The photoresist MicroChem® SPR220-3.0 was selected as the masking material for subsequent bulk micromachining process for its thickness of 3µm. It both resolvess our finest features of 6µm and is thick enough to withstand the silicon etching media. The hard baking procedure needs to ramp up and down the temperature to avoid cracks on the photoresist surface. The substrate was bulk micromachined by the Deep Reaction Ion Etching (DRIE) process to carve the shape of the microrobot. The etching rate was estimated by profilometry and the reflective microscopy was used to verify completion of the process by checking if the smallest etching target, the release holes, are reflecting light and appear bright at end of etch. Before release, a thorough oxygen plasma cleaning of the substrate is necessary since it removes the passivation chemicals that may impede releasing process. Releasing was performed on the die scale in the anhydrous Hydrogen Fluoride etcher for one hour.

B. Microassembly of SerpenBot

The SerpenBot was assembled by NEXUS microassembly system in several steps. The NEXUS microassembly system, Figure 7c, has two motorized manipulators M_1 and M_2 . The M_1 holds the vacuum secured sample chuck and provides three degrees of freedom: translational $X,\,Y,\,$ and rotation. The end-effector, which is a vacuum tip, is mounted on the M_2 manipulator. M_2 has five degrees of freedom, a manual Z stage at the bottom provides a height adjustment base, four motorized stages on top of Z consist of $X,\,Y,\,Z,\,$ and rotation. The rotation stage is mounted on the sidewall of the last stage and the vacuum tip is fixed on it through a 3D-printed fixture.

The goal of this process is to assemble a $60\mu m \times 60\mu m$ square or $60\mu m$ diameter dimple onto the body of the SerpenBot, as shown in Figure 7a and Figure 7b. Since the dimple is smaller than the vacuum tip's diameter of 150 μm , a dimple handle, is designed so that it can be picked up by the tip. The dimple is attached to the handle frame by a $6\mu m$ wide $55\mu m$ long neck, which allows easy break after assembly.

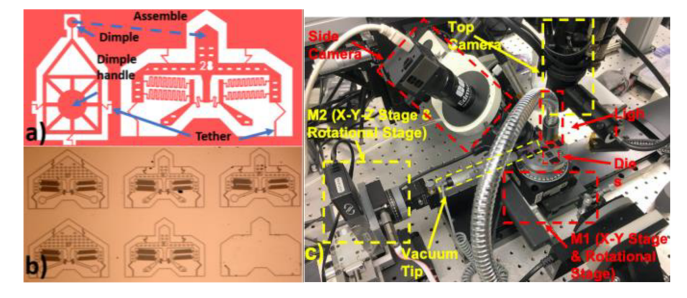
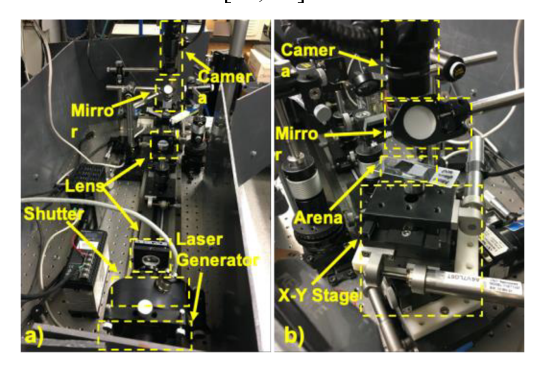


Figure 7. a) Illustration of the dimple and the SerpenBot body. b) Tethered SerpenBot on a Silicon die. c) The NEXUS microassembly system.

The dimple with its handle was first set free by breaking all the tethers holding them. Then, it was picked up by the vacuum tip and the dimple was dipped into a pool of UV adhesive. The dimple then aligned with the assembly site on the SerpenBot's body and lowered on it to make contact. A Ultraviolet (UV) flashlight was then used to cure the adhesive and break the neck after the glue solidifies. And eventually, the tethers holding the SerpenBot were broken and the microrobot was flipped to conclude the process.

C. Locomotion Experimental Setup

To experimentally validate the SerpenBot, we utilize a laser power delivery instrument that includes a laser source, camera, and motorized stages shown in Figure 8. The laser spot is delivered on the center of the microrobot substrate and further aligned with the center of the camera's view. A motorized stage maintains the microrobot under the laser spot through visual feedback of the microscope camera. More details about our experimental conditions and servoing controller can be found in [10, 16].



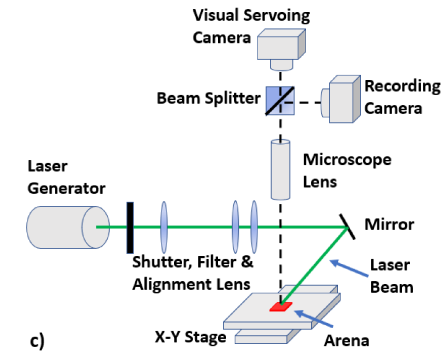


Figure 8. a) and b) show different views of the experimental setup. c) schematic diagram of the experimental setup used to power microrobots.

V. RESULTS AND DISCUSSION

A series of experiments were conducted in order to experimentally validate the proposed SerpenBot design, and confirm its steering ability. Assembled SerpenBots with a reduced frame mass were fabricated, assembled, and placed on a clean Si substrate as depicted in Figure 9. The SEM images show two slightly different microrobots in leg design, referred to as design No.28 and No.29. These sample microrobots were exposed to a pulsed laser with repetition rate swept in a range until the robot's motion was observed. Due to the different boundary conditions of an untethered microrobot compared to simulation boundary conditions we observed that differential resonance was achieved at much lower frequencies as expected, with experimental results shown in Table IV.

The discrepancy between the calculated resonant frequency of the ETA shown in Table III) and values determined experimentally in Table IV is due to the boundary conditions difference between simulation and experimental scenarios. As noted in section II, the model of ETA is significantly idealized as it is very difficult to simulate motion of the untethered microrobot's leg on the substrate. On other hand, we do not have direct evidence that experimental

frequencies collected in Table IV are the actuator's resonance frequencies for two untethered SerpenBots on the Si surface.

TABLE IV. SERPENBOT'S EXPERIMENTAL OPERATION FREQUENCY

No.	Forward/Backward Frequency (Hz)	Left Frequency (Hz)	Right Frequency (Hz)
28	1000	600	1700
29	1100	2000	700

In the first set of measurements, we tested multiple SerpenBots with slightly different frame and leg designs, in order to see which robot had reasonable maneuverability. The overall size of SerpenBot is less than 1mm and the mass is in the microgram level, so it is sensitive to the spring and frame design. In conclusion we see that little frame and actuator design differences will bring significant performance differences. Results show that design No.28 and No.29 were the most responsive to laser actuation (Figure 9). No.28 and No.29 robots have essentially the same design of the body, with a mass 0.71 times lower than the initial design in Figure 6 and differing only in the shape of the legs.

A second series of experiments were conducted to realize motion and steering of the microrobots in a controlled way with the No.28 and No.29 SerpenBot designs. We tested several samples from each design to verify that the results were repeatable and consistent. During our experiments, the laser was operated in the burst mode, where each burst had 15 to 25 pulses with a 300 ms delay. The average power was in the range of 70 – 200 mW. The laser repetition frequency f was varied in the range between 500 - 5000 Hz in order to determine the f values that enables specific type of the robot's motion: forward, backward, left turn, and right turn. Robot No.28 always moves in the arrow direction shown in Figure 9 (forward), while robot No.29 always moves in the arrow direction backward. Both robots have frequency sensitive turning and driving behavior with 3 different f values, allowing controlled steering and motion along a straight trajectory on a silicon substrate (Table IV).

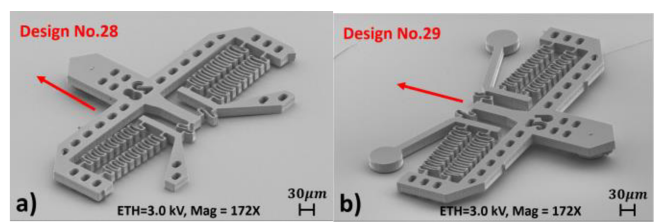


Figure 9. Scanning Electron Microscope images of SerpenBot designs 28 and 29, where the red arrows indicate direction (orientation) of motion.

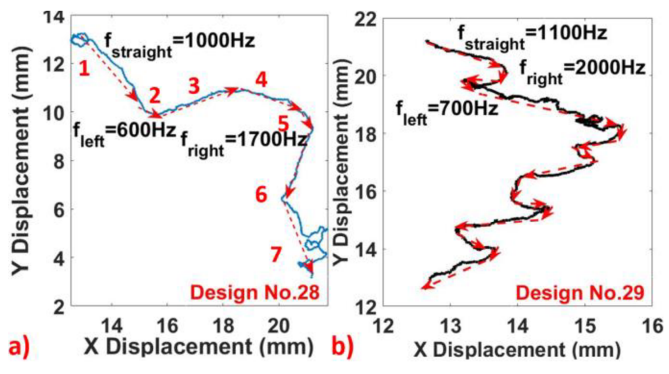


Figure 10. Planar steering trajectories with microrobots No.28 and No.29.

For microrobot trajectory shown in Figure 10(a), we can describe motion and steering mechanism of the given SerpenBot by referring to each of the 7 marked sections:

- 1) The robot is initially at rest and starts to move forward upon exposure to the laser with mod. freq. f = 1000 Hz.
- 2) Change f to 600 Hz robot turns left $\sim\!45^{\circ}$ small curve radius.
- 3) Change f to 1000 Hz robot moves in forward direction.
- 4) Change f to 1700 Hz robot turns right gradually \sim 180° large curve radius.
- 5) Change f to 1000 Hz robot moves in forward direction.
- 6) Change f to 600 Hz robot turns left $\sim 90^{\circ}$ small curve radius
- 7) Change f to 1000 Hz robot moves in forward direction.

Using this sequence of laser frequencies, SerpenBot can be steered by switching the modulation frequency of the laser between three values. The same level of control was achieved for the microrobot No.29 but naturally with a different set of frequency values – due to different geometry of the actuators and leg shapes (Figure 9). The shape of the recorded trajectory of the No.29 robot reveals that described steering control for this robot is also repeatable. It is can be seen in Figure 10 that similar maneuvers (turns) are repeated by the SerpenBot several times. The velocity of the robot can be controlled by the light intensity of the pulsed laser. For our experiments, the average forward/backward velocity was 68 microns/s and 57 microns/s respectively, the turning angular velocity was 2.3 °/s and 3.8 °/s.

VI. CONCLUSION AND FUTURE WORK

In this paper, we have introduced a new type of thermal actuator, Elbow Thermal Actuator (ETA) for SerpenBot - a laser-driven MEMS microrobot. Applying theoretical analysis and simulation we determined that the leverage mechanism of this type of thermal actuator can enhance thermal expansion to achieve larger static displacement. By tuning the geometric parameters of the actuator, such as lengths, widths, and number of serpentine turns, we can achieve different resonant frequencies of the actuator in a dynamic scenario, and design microrobots with different leg responses.

We have experimentally validated our differential leg dynamic models by illuminating SerpenBots with different laser frequencies through a customized laser and visual servoing tracking experimental instrument. The position of the microrobot was tracked while laser pulse frequencies were swept in a wide range. Results show that it is possible to achieve locomotion and steering control of the robot by tuning the laser frequency. We have determined experimental frequencies needed to realize locomotion and steering control for two different microrobot designs and verified that the resulting motions are repeatable.

In future work we will focus on implementing closed-loop motion controllers for microrobot steering along planned trajectories by tuning the laser driving frequency, spot intensity and position.

ACKNOWLEDGMENT

This work was supported by National Science Foundation Grant #CMMI 1734383. We wish to thank the Micro Nano Technology Center (MNTC) staff at the University of Louisville, for their help with cleanroom fabrication, Brooke Hall and Piper Cannon who helped assemble and simulate the SerpenBot.

REFERENCES

- S. Miyashita., S. Guitron, S. Li and D. Rus, "Robotic metamorphosis by origami exoskeletons," *Science Robotics* 27 Sep 2017: Vol. 2, Issue 10
- [2] M.A, Rahman, J. Cheng, Z. Wang and A.T Ohta, "Cooperative micromanipulation using the independent actuation of fifty microrobots in parallel," *Scientific Reports* volume 7, Article number: 3278 (2017).
- [3] B. J. Nelson, I. K. Kaliakatsos and J. J. Abbott, "Microrobots for minimally invasive medicine." *Annual Review of Biomedical Engineering*, vol. 12, no. 1, p. 55, 2010.
- [4] P. Ryan and E. Diller, "Magnetic Actuation for Full Dexterity Microrobotic Control Using Rotating Permanent Magnets," *IEEE Transactions on Robotics*, vol. 33, no. 6, pp. 1398-1409, 2017.
- [5] C. Elbuken, M. B. Khamesee and M. Yavuz, "Magnetic levitation as a micromanipulation technique for MEMS," 2009 International Conference on Mechatronics and Automation, Changchun, 2009, pp. 955-959.
- [6] B. Goldberg, R. Zufferey, N. Doshi, E. F. Helbling, G. Whittredge, M. Kovac, and R. J. Wood, "Power and Control Autonomy for High-Speed Locomotion With an Insect-Scale Legged Robot," in *IEEE Robotics and Automation Letters*, vol. 3, no. 2, pp. 987-993, April 2018.
- [7] R. Murthy, A. N. Das and D. O. Popa, "ARRIpede: A stick-slip micro crawler/conveyor robot constructed via 2 ½D MEMS assembly," 2008 IEEE/RSJ International Conference on Intelligent Robots and Systems, Nice, 2008, pp. 34-40.
- [8] J. James, V. Iyer, Y. Chukewad, S. Gollakota and S. B. Fuller, "Liftoff of a 190 mg Laser-Powered Aerial Vehicle: The Lightest Wireless Robot to Fly," 2018 IEEE International Conference on Robotics and Automation (ICRA), Brisbane, Australia, May 21-25, 2018.
- [9] M. R. Pac and D. O. Popa, "3-DOF untethered microrobot powered by a single laser beam based on differential thermal dynamics," 2011 IEEE International Conference on Robotics and Automation, Shanghai, 2011, pp. 121-127.
- [10] R. Zhang, A. Sherehiy, Z. Yang, D. Wei, C. K. Harnett and D. O. Popa, "ChevBot – An Untethered Microrobot Powered by Laser for Microfactory Applications," 2019 International Conference on Robotics and Automation (ICRA), Montreal, QC, Canada, 2019, pp. 231-236.
- [11] J. Varona, M. Tecpoyotl-Torres and A. A. Hamoui, "Polysilicon vertical actuator powered with waste heat," 2008 IEEE Custom Integrated Circuits Conference, San Jose, CA, 2008, pp. 519-522.
- [12] G. Barillaro, A. Molfese, A. Nannini, F. Pieri, (2005), "Analysis, simulation and relative performances of two kinds of serpentine springs." *Journal of Micromechanics and Microengineering*. 15. 736.
- [13] A. Ghisi, S. Mariani. "Effect of Imperfections Due to Material Heterogeneity on the Offset of Polysilicon MEMS Structures," *Sensors* (Basel). 2019;19(15):3256, July 2019.
- [14] Liu, Y. F., Li, J., Zhang, Z. M., Hu, X. H., and Zhang, W. J.: Experimental comparison of five friction models on the same test-bed of the micro stick-slip motion system, *Mech. Sci.*, 6, 15-28, 2015.
- [15] D.O. Popa, B.H. Kang, J.T. Wen, H.E. Stephanou, "Dynamic modeling and input shaping of thermal bimorph MEMS actuators," in *IEEE International Conference on Robotics and Automation*, Taipei, 2003.
- [16] Z. Yang, M. N. Saadatzi, R. Zhang, A. Sherehiy, D. Wei, C. K. Harnett, and D. O. Popa, "Multiphysics Dynamic Model Validation Methodology for Laser-Driven Microrobots," 2019 IEEE 15th International Conference on Automation Science and Engineering (CASE), Vancouver, BC, Canada, 2019, pp. 1555-1561.